

Inhomogeneous Jets from Neutron Star Mergers: One Jet to Rule them all

Gavin P. Lamb¹*, Lorenzo Nativi², Stephan Rosswog², D. Alexander Kann³, Andrew Levan⁴, Christoffer Lundman², & Nial Tanvir¹.

¹*School of Physics and Astronomy, University of Leicester, University Road, Leicester LE1 7RH, UK*

²*The Oskar Klein Centre, Department of Astronomy, Stockholm University, AlbaNova, SE-10691 Stockholm, Sweden*

³*IAA-CSIC, Glorieta de la Astronomía, s/n, 18008 Granada, Spain*

⁴*Department of Astrophysics, Radboud University, 6525 AJ Nijmegen, The Netherlands*

Accepted XXX. Received YYY; in original form ZZZ.

ABSTRACT

The broad, ~ 4 order of magnitude range in energy, inferred via afterglow observations, for the short Gamma-Ray Burst (GRB) population is difficult to reconcile with the narrow energy distribution expected from neutron star merger progenitors. Using the resultant profiles from 3D hydrodynamic simulations of relativistic jets interacting with neutron star merger wind ejecta, we show how the inhomogeneity of energy and velocity can alter the observed afterglow lightcurve. From a single jet we find that the peak afterglow flux depends sensitively on the observer’s line-of-sight: at an inclination within the GRB emitting region we find peak flux variability on the order < 0.5 dex through rotational orientation, and < 1.3 dex for polar inclination. The inferred jet kinetic energy for a fixed parameter afterglow covers $\sim 1/3$ of the observed short GRB population. We find a physically motivated, analytic jet structure function via our simulations and include an approximation for the varying collimation due to the merger ejecta mass. We show that by considering the observed range of merger ejecta masses, a short GRB jet population with a single intrinsic energy is capable of explaining the observed broad diversity in short GRB kinetic energies.

Key words: gamma-ray burst: general – transients: neutron star mergers – gamma-ray bursts

1 INTRODUCTION

Afterglows following short duration Gamma-Ray Bursts (GRBs) are powered by decelerating, relativistic jets. The jet parameters inferred via afterglow studies reveal a diverse population in terms of energy, microphysics, and environment (Fong et al. 2015; O’Connor et al. 2020). This broad range in energy can be difficult to reconcile with the likely progenitor systems for these events; the mergers of either neutron star binaries, or black hole-neutron star binaries (see Nakar 2007; Berger 2014; D’Avanzo 2015, for a review of short GRBs). For such a compact binary merger origin, the power available for the jets is expected to be on the order of 10^{51} erg s^{−1}, and have quite a narrow distribution (Shapiro 2017; Fryer et al. 2019).

A jet launched following a compact stellar merger will propagate through the merger ejecta and winds (e.g., Aloy et al. 2005; Nagakura et al. 2014; Duffell et al. 2015; Murguia-Berthier et al. 2017; Geng et al. 2019; Nathanail et al. 2021; Nativi et al. 2021, 2022; Pavan et al. 2021; Urrutia et al. 2021), this results in the collimation of the jet before breakout (Bromberg et al. 2011; Salafia et al. 2020; Hamidani & Ioka 2021). As a consequence of the turbulent motions arising during the hydrodynamic interaction between the jet and the surrounding ejecta, the resultant jet will have an angular shape that is independent of the injected jet structure (Nativi et al. 2022), unless the ejecta density is very low or the jet power very high (Urrutia et al. 2021).

As GRBs are highly beamed, their afterglows are preferentially

selected to be at small inclination angles to the line-of-sight i.e., where the emission is brightest (Beniamini & Nakar 2019). For such GRBs, the afterglow lightcurve can be modelled using a simple top-hat jet structure, where any angular dependence of the energy or velocity is ignored, resulting in a uniform jet within a cone defined by the jet’s opening angle (see discussion in Aksulu et al. 2021). However, the energy inferred from afterglow lightcurve fits, where a top-hat jet structure is assumed, will return a kinetic energy equal to the highest energy with a beaming cone, $1/\Gamma$ – where Γ is the bulk Lorentz factor of the emitting region at the observation time, within the observers line-of-sight at \sim the peak time and not the true energy of the jet. Here we use the results of 3D hydrodynamic simulations of jets propagating through the merger ejecta and neutrino-driven winds of a neutron star merger (see, Perego et al. 2014; Nativi et al. 2021, 2022) to investigate the effects of inhomogeneity within the jet’s energy and velocity profile on the afterglows of short GRBs.

In §2 we describe our method for modelling the resultant jet profiles from the simulations relevant to the bright GRB emitting population of short bursts. In §3 we show the diversity of afterglow lightcurves from a single jet simulation as a function of observer line-of-sight relative to both inclination and rotation. Additionally, we use the simulation jet structure results to generate a general, analytic function for the typical structure of a short GRB jet and compare the flux density for the afterglow from this model to the short GRB afterglow population. These results are discussed in §4, where we approximate how the ejecta mass responsible for a thermal kilonova (e.g., Rosswog et al. 1999; Hotokezaka et al. 2013) can alter the effective core-size of the jet and show how this compares to a selec-

* E-mail: gpl6@le.ac.uk

tion of typical afterglow lightcurves for short GRBs with candidate kilonovae. Our conclusions are listed in §5.

2 METHOD

The energy per steradian and Lorentz factor at each point of a surface that describes the afterglow-producing jet can be extracted from simulations. We use two ultra-relativistic jet simulations from [Nativi et al. \(2022\)](#), and determine the typical Lorentz factor for each surface element from the mass-averaged radial profile for $h\Gamma > 2$ at a given polar angle, θ , and rotational angle, ϕ – where h is the specific enthalpy, and Γ the Lorentz factor. The two simulations we utilise are identical but for the structure of the injected jet in each case; the first uses a ‘top-hat’ structured jet with a uniform energy and enthalpy until a sharply cut-off edge, and the second uses a profile described by a Gaussian function. Both jets have a power, $L_j \sim 10^{50}$ erg s $^{-1}$, and are labelled **th50** and **gs50** respectively.

The two left panels in Figure 1 show the face-on distribution of energy and Lorentz factor for each simulation output once ballistic expansion is achieved i.e., $(h - 1) < 1$ everywhere on the grid. The right panels show energy (red) and Lorentz factor (blue) with polar angle where the shaded regions indicate the maximum to minimum range for each parameter with rotation through ϕ on the jet surface at the given angle θ . We can approximate these profiles analytically using (e.g. [Beniamini et al. 2020](#)):

$$\Theta = \left[1 + \left(\frac{\theta}{\theta_c} \right)^2 \right]^{1/2}, \quad (1)$$

$$E(\theta) = E(\theta = 0)\Theta^{-a}, \quad (2)$$

$$\Gamma(\theta) = 1 + [\Gamma(\theta = 0) - 1]\Theta^{-b}. \quad (3)$$

We use a linear regression fit to the mean for both the energy and Lorentz factor profiles within an angle $\theta_j = 0.42$ rad, or $\sim 24^\circ$. The energy profile is cut-off¹ using the functional form $(1 + (\theta/\theta_j)^{a_2})^{-a_1}$. The model jet structure fit parameters are shown in Table 1.

The emission of γ -rays from a jet requires the source to be optically thin which places physical constraints on the angular profile from which a GRB can be emitted/observed (e.g. [Lamb & Kobayashi 2017](#)). Viable locations for γ -ray emission can be determined using a relation between energy and Lorentz factor that considers the opacity of the medium to gamma-rays. The minimum Lorentz factor for an optically thin medium considering only the scattering by electrons that accompany baryons in the jet is (e.g. [Lithwick & Sari 2001](#); [Matsumoto et al. 2019](#)):

$$\Gamma_{\min} = \left(\frac{\sigma_T}{32m_p\pi c^4} \frac{L_{\gamma,\text{iso}}(1+z)}{\delta t} \right)^{1/6}, \quad (4)$$

which is consistent with $\Gamma_{\min} \propto E_{\gamma,\text{iso}}^{0.17}$ found in [Lamb & Kobayashi \(2016\)](#). Here, σ_T is the Thompson cross-section, m_p is the mass of a proton, c is the speed of light, and the variables: $L_{\gamma,\text{iso}}$ is the isotropic equivalent γ -ray luminosity, z is the source redshift, and δt is the minimum variability timescale. The observed isotropic equivalent γ -ray energy can be approximated from the luminosity

as, $E_{\gamma,\text{iso}} = L_{\gamma,\text{iso}}T_{\text{dur}}$, where T_{dur} is the burst duration². The total energy is then $E = E_{\gamma,\text{iso}}/\eta$, where η is the efficiency of the γ -ray emission. The maximum energy per steradian for the outflow with a given Γ to be γ -ray bright is then

$$\frac{E}{\Omega} \sim \left(\frac{\Gamma}{10} \right)^6 \left(\frac{\delta t}{0.1\text{s}} \right) \left(\frac{T_{\text{dur}}}{0.1\text{s}} \right) \left(\frac{\eta}{0.15} \right)^{-1} \times 10^{48} \text{ erg/sr}, \quad (5)$$

where all timescales are measured in the lab frame.

To test how the inhomogeneity of these jet surfaces affect the afterglow lightcurves for various observers, we generate afterglows at a fixed emission frequency for observers at various inclinations and rotations with respect to the outflow. The afterglows are calculated using the method described in [Lamb & Kobayashi \(2017\)](#); [Lamb et al. \(2018, 2021\)](#). The lightcurves for each ϕ element at a polar angle $\theta = [0.0, 0.3, 0.7, 1.0, 1.5, 2.0, 3.0, 4.0, 5.0, \& 6.0] \times \theta_c$ for the two simulation models are shown in Figure 2. The lightcurves are calculated at an observed frequency, $\nu = 3.8 \times 10^{14}$ Hz, where for simplicity we assume redshift, $z = 0$, and a luminosity distance, $D_L = 100$ Mpc. The afterglow model microphysical parameters are fixed at $\epsilon_e = \sqrt{\epsilon_B} = 0.1$, an electron distribution index, $p = 2.15$, an ambient medium particle number density, $n = 1 \text{ cm}^{-3}$, and a γ -ray efficiency of $\eta = 0.15$.

3 RESULTS

We have generated afterglow lightcurves for observers at various θ and ϕ relative to the jet central axis for the resultant energy and Lorentz factor surface profiles from two 3D hydrodynamic simulations of jets propagating through neutron star merger winds (see [Nativi et al. 2021, 2022](#), for simulation details). The effects of the jet orientation to the line-of-sight on the peak afterglow flux, for emission in the regime $\nu_m < \nu < \nu_c$, where ν_m is the characteristic synchrotron peak frequency and ν_c is the cooling frequency, is shown in Figure 3 for observers within the γ -ray emitting region of the jet. The maximum variation in the peak flux at a fixed inclination but through a 2π rotation in ϕ is ~ 0.5 dex seen for the **gs50** model. The **th50** model has less overall variation, with ~ 0.2 dex in peak afterglow flux. The most significant change in peak flux is seen with inclination from the jet central axis, where for both **th50** and **gs50** the peak flux varies by ~ 1.3 dex within the γ -ray emitting region.

For GRB afterglows, the kinetic energy of the jet is found via afterglow modelling which typically assumes an outflow with a uniform energy distribution (e.g. [Fong et al. 2015](#)). The results of our simulations show that the jets that produce GRB afterglows do not have a uniform energy profile, and that orientation through both θ and ϕ can change the kinetic energy inferred from simple afterglow models. For GRB afterglows with $\nu_m < \nu < \nu_c$ the peak flux is $F_p \propto E_k^{(3+p)/4}$, where F_p is the afterglow peak flux, E_k is the kinetic energy, and p is the power-law distribution index for accelerated electrons ([Sari et al. 1998](#)). Figure 4 shows the kinetic energy distribution, as inferred by a distant observer and weighted for a randomly oriented source with inclination $\iota \leq \theta_j$, for each of our jet simulations in comparison to the observed kinetic energy distribution for the population of short GRBs as listed in [Fong et al. \(2015\)](#). The afterglow lightcurves were calculated assuming a fiducial efficiency for γ -rays of $\eta = 0.15$, where the energy in the jet is $E = E_\gamma + E_k$, with E_γ being the energy radiated in γ -rays. The dashed histogram shows the distribution

¹ The wide angle cut-off in energy for the simulation profiles is a result of the radial averaging process where we only sample components with $h\Gamma > 2$. The contribution to the observable afterglow from wider, lower energy and Γ regions is negligible, see [Nativi et al. \(2022\)](#) for details.

² For an aligned observer, $\iota = 0$, the GRB duration is equivalent to the engine duration; for our simulation this is 0.1 s

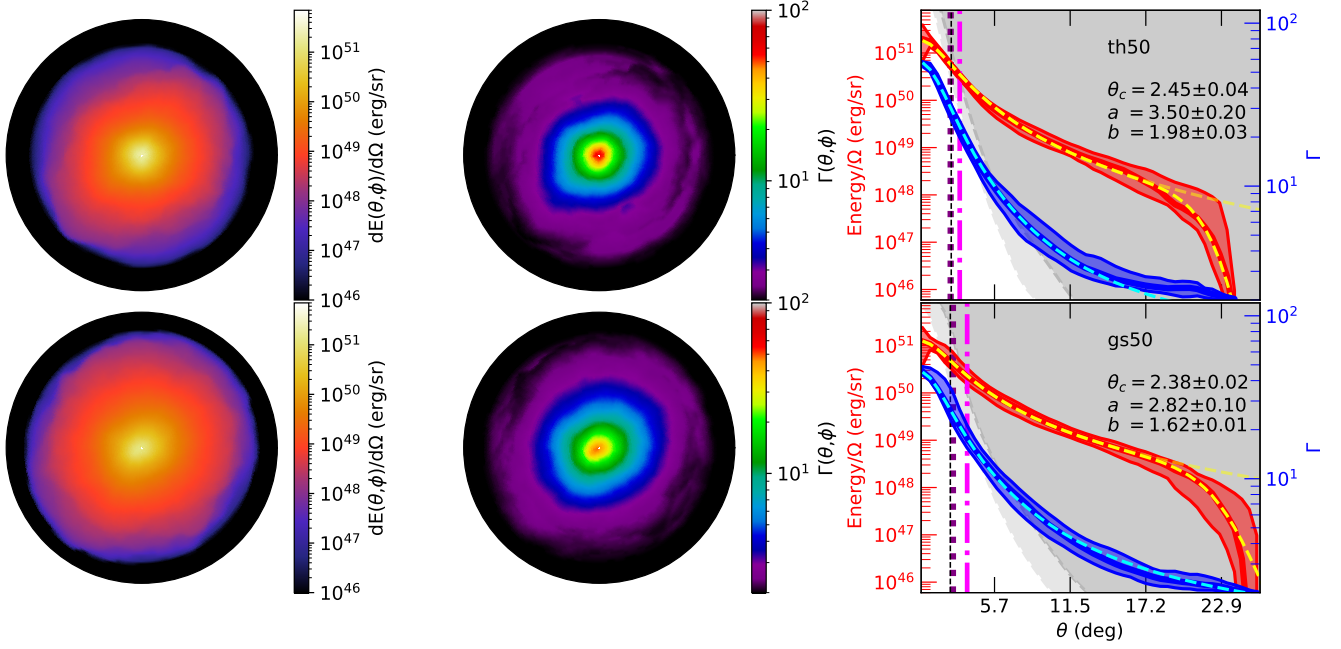


Figure 1. [Polar-plots] Face-on projections of the resultant jets/outflows. From the centre, $\theta = 0$, to the edge, $\theta = 29^\circ$. Each row indicates a different initial jet structure described by: th50, gs50, top to bottom. Where th indicates a top-hat profile for the injected jet structure, gs indicates a Gaussian structure, and the number is the logarithm of the jet power i.e., 10^{50} erg s $^{-1}$. **[Left]:** The energy per steradian (erg sr $^{-1}$) for the resultant jet profiles. Energy per steradian is shown in the range $1 \times 10^{46} \leq E/\Omega \leq 7 \times 10^{51}$ erg sr $^{-1}$. **[Centre]:** The resultant mass-averaged Lorentz factor for the same projection. Bulk Lorentz factor is shown in the range $2 \leq \Gamma \leq 100$. **[Right]** The maximum and minimum energy per steradian (red) and Lorentz factor (blue) in rotation at each angle θ from the central axis for each model. The largest logarithmic variations are seen at wider angles where energies and Lorentz factors are lower – the average value is shown as a thick line within the shaded region. The purple, vertical dotted line indicates the jet opening angle as inferred by the afterglow break time for an on-axis observer – the black dashed line is the core opening angle found via fits to the mean angular profile, showing good agreement with the values inferred via the jet break (Nativi et al. 2022). The grey shaded area indicates the region within which we don’t expect detectable γ -ray emission due to opacity arguments, see equation 5, where we have assumed $\eta = 0.15$, $T_{\text{dur}} = 0.1$ s, and $\delta t = 0.1$ s – the lighter grey region indicates the limit using the minimum Γ value, while the darker region indicates the limit using the maximum Γ value for each angular segment. The pink, dash-dotted line indicates the maximum angle for γ -ray emission considering only the opacity due to electrons that accompany baryons in the jet. The yellow dashed line indicates the approximate functional shape of the jet profile in terms of energy with the fainter line at wider angles showing the profile without the energy cut-off, while the cyan dashed line represents the Lorentz factor profiles – the fit values for θ_c , a and b in each panel are those for the analytic function in equations 1–3 (see text for details).

Table 1. Analytic jet structure profile parameters, see equations 1–3 plus text, from fits to the mean energy and Lorentz factor with polar angle for each simulation and the averaged profile, see §3.

Model	θ_c (rad)	$\log(E_c)$ (log erg sr $^{-1}$)	Γ_c	a	a_1	a_2	b
th50	0.0428 ± 0.0007	51.27 ± 0.11	58.0 ± 0.2	3.50 ± 0.20	7.89 ± 0.94	14.79 ± 3.14	1.98 ± 0.03
gs50	0.0415 ± 0.0004	51.10 ± 0.06	45.6 ± 0.1	2.82 ± 0.10	3.96 ± 0.45	12.48 ± 2.59	1.62 ± 0.01
Averaged	0.0424 ± 0.0005	51.18 ± 0.08	52.3 ± 0.2	3.10 ± 0.14	3.64 ± 0.54	10.90 ± 3.02	1.82 ± 0.02

assuming an efficiency, $\eta = 0.85$, resulting in a lower typical energy distribution as more energy is lost via the GRB. The dash-dotted lines show the isotropic equivalent kinetic energy for each of our jets assuming that all of the injected energy is contained within a solid angle section defined by the jet structure core angle listed in Table 1. The logarithmic kinetic energy distribution inferred from a single jet model covers \sim third of the observed short GRB population. As we have artificially fixed the γ -ray efficiency for the entire emitting region, our distribution is likely significantly narrower than one with a more realistically determined efficiency e.g., $\eta(\theta, \phi)$, that varies according to local conditions across the jet’s surface.

The two 3D simulations highlight that the form of the resultant jet profiles are largely a result of fluid instabilities in the jet-wind interaction regions (Nativi et al. 2022), however, for lower density

winds³, or much more powerful jets, the injected jet structure can be partially preserved (Urrutia et al. 2021). By using the rotation in ϕ for each surface to produce an energy and Lorentz factor profile in θ we can find an average jet structure profile from our simulations. We bootstrap these unique profiles to find a mean jet structure, and fit equations 1–3, plus the energy cut-off described in §2, via linear regression to find the best-fit parameters. These are listed in Table 1 as ‘Averaged’ and shown in Figure 5 along with the initial profiles.

The afterglows from our averaged jet structure profile are com-

³ The density and mass of the merger winds in the simulations of Nativi et al. (2021, 2022) are already low and the emergent jet structure did not preserve the injected profile. We do not expect many physical scenarios where the injected jet’s structure contributes significantly to the emergent jet profile.

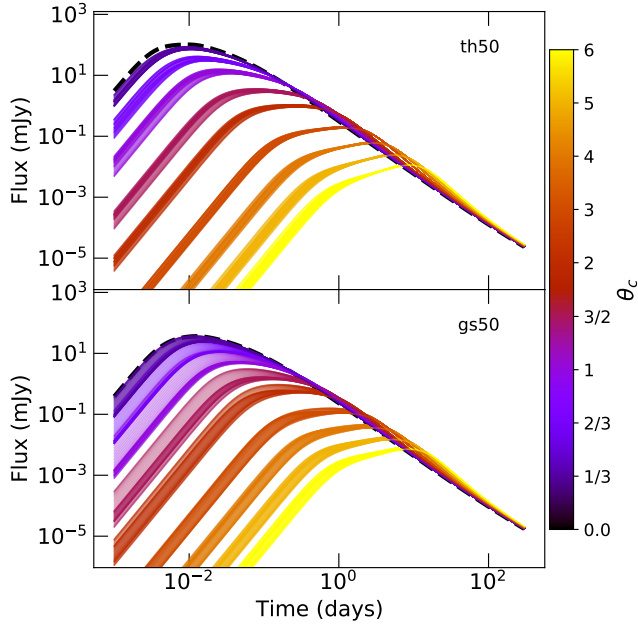


Figure 2. Lightcurves at various polar angles, θ , from the jet axis as a fraction of the effective core angle for each profile, where the line colour indicates the relative angle. The effective core angles are given in Table 1. At each θ , lightcurves at all available rotational orientations, ϕ , are shown in the same colour, and the apparent broadness of the lines represents the spread in flux as a result of the rotational orientation. For a fixed inclination angle, the rotational orientation of the system has a significant effect on the flux density at \sim peak time, or equivalently the deceleration time, for an observer $\iota \lesssim \theta_c$. Where $\iota \gtrsim 2\theta_c$, then only the early and pre-peak lightcurve is sensitive to the rotational orientation.

pared to the observed short GRB population in Figure 6. Here we show, in red, the model R_C -band afterglow for a source at $z = 1$ using the same fiducial parameters as the earlier models. Individual lightcurves are shown for an observer that is either aligned with the jet central axis, or at $\iota = \theta_\gamma$, the maximum angle at which γ -rays are emitted for our model; these cover the range of expected GRB afterglows from a jet with our structure and fixed parameters. The sample of 30 individual short GRBs (grey and coloured lines) are optical afterglows for bursts with a measured redshift; each afterglow is a composite of various filters that have been shifted using the spectral energy distribution for each burst and corrected for Galactic foreground extinction and host contribution (if necessary and possible) to produce an observed R_C -band lightcurve for a source at redshift $z = 1$ (see Kann et al. 2011; Agüí Fernández et al. 2021, and references therein).

The post-jet-break decline for our model lightcurves is consistent with the tail of the short GRB population, and the peak of the model afterglows agrees nicely with the brightest in this distribution – we note that short GRB afterglows shown here may include contributions from extended prompt emission, the reverse shock, energy injection, and kilonova. Our afterglow models have a fixed ambient density, $n = 1 \text{ cm}^{-3}$, and microphysical parameters, $\epsilon_e = \sqrt{\epsilon_B} = 0.1$ and $p = 2.15$; allowing these to vary would change both the timescale and the peak flux of the afterglow, with the deceleration (or peak) time, $t_d \propto E_k^{1/3} n^{-1/3} \Gamma^{-8/3}$, and $F_p \propto E_k \Gamma^{2(p-1)} \epsilon_B^{(1+p)/4} \epsilon_e^{p-1} n^{(1+p)/4}$, where Γ is the bulk Lorentz factor at the deceleration radius and the emitting frequency is in the regime, $\nu_m < \nu < \nu_c$.

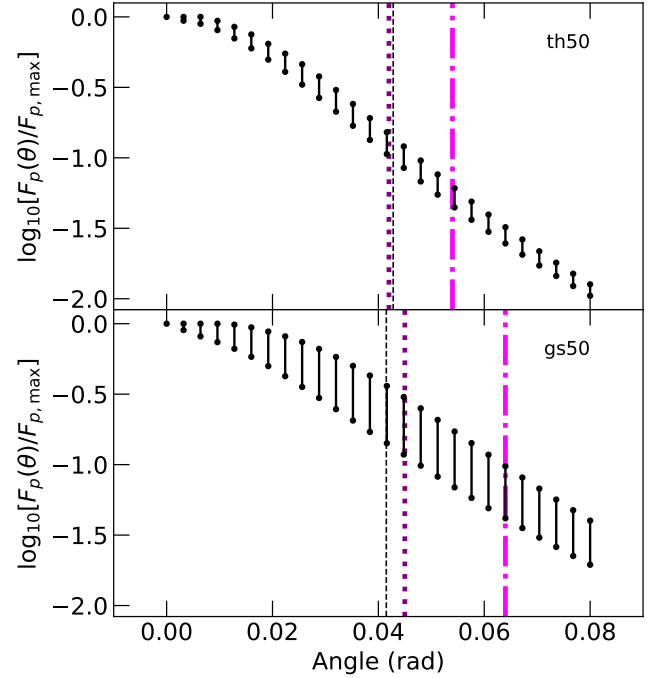


Figure 3. The range in afterglow peak flux values relative to the maximum afterglow peak flux through rotation in ϕ of the jet at a fixed polar angle within the γ -ray bright jet region for each structure profile. The purple dotted vertical line indicates the inferred jet opening angle for an on-axis observer, given the jet break time; the black dashed line indicates the jet core angle from mean jet profile fits; and the pink dash-dotted line indicates the maximum angle at which the jet is optically thin to γ -rays.

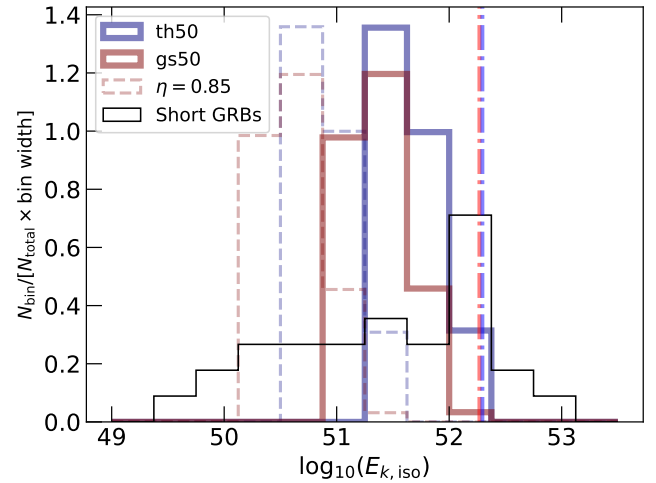


Figure 4. Probability density of the kinetic energy from our model jet structure profiles inferred from the peak afterglow flux, versus the observed short GRB kinetic energy distribution as listed in Fong et al. (2015) for $\epsilon_B = 0.01$. For a fixed γ -ray efficiency ($\eta = 0.15$), a single jet profile can account for \sim one third of the observed logarithmic kinetic energy distribution range – the distribution with a fixed $\eta = 0.85$ is shown as a dashed line. The dash-dotted lines indicate the isotropic equivalent energy for each jet assuming the intrinsic jet energy, $E_j \sim 10^{49}$ erg, is contained within a cone defined by the jet structure profile core angle.

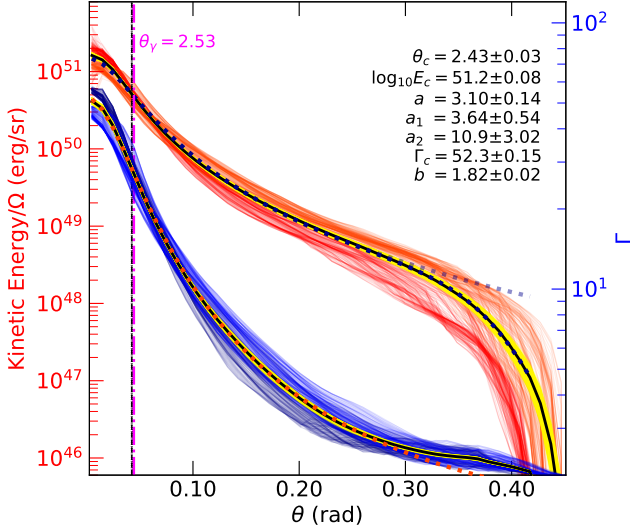


Figure 5. The energy (left axis) and Γ (right axis) profiles at each rotation step in ϕ for both the th50 (red/dark-blue) and gs50 (orange/blue). By assuming that the differences in these model profiles are the result of chaotic mixing processes while the jet propagates through the neutron star merger ejecta, we use a bootstrap to find the average profile (yellow are individual bootstrap means, black gives the distribution mean). We then fit our analytic jet structure profile for $0.0 \leq \theta \leq 0.42$ rad to the distribution mean – the analytic model fit parameters are shown in the figure, and the profiles are indicated with a dotted line for both the energy and Γ .

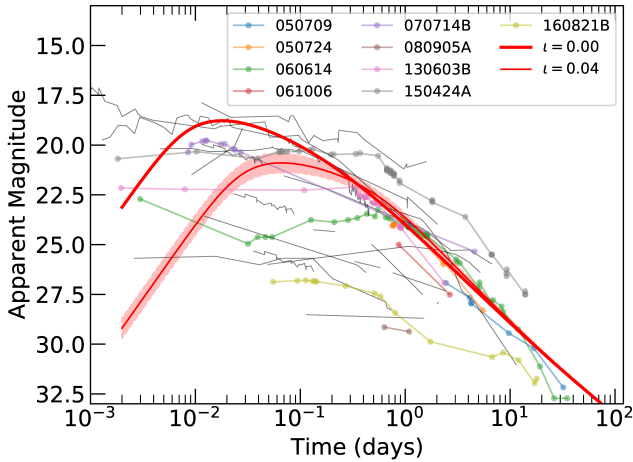


Figure 6. The averaged model afterglow lightcurve range for observers within the γ -ray bright angle, θ_γ ; red lines indicate the afterglow viewed at an inclination $\iota = 0$, and the widest angle for γ -ray emission, where the shaded region includes the maximum variability in peak flux expected due to the rotational orientation of the jet. The short GRB afterglows within our sample are shown as thin grey lines, and coloured lines with points marking data for short GRBs with candidate kilonovae. All lightcurves have been normalised to a redshift, $z = 1$, for consistency. Whereas the model lightcurves have a fixed ambient medium, $n = 1 \text{ cm}^{-3}$, much of the diversity in the observed short GRB afterglows can be accounted for by varying ambient medium density values between events. This suggests that the intrinsic energy distribution of short GRB jets is quite narrow with environmental effects determining much of the population scatter.

4 DISCUSSION

We have used the results from 3D hydrodynamic simulations of relativistic jets interacting with neutron star merger winds to show the effect on the observed afterglow, in terms of the peak flux, from the inhomogeneity of the resultant jet structure in both polar, θ , and rotational, ϕ , orientations. We have shown that for an observer viewing the jet at $\iota \leq \theta_\gamma$, the rotational orientation of the jet surface, $0 \leq \phi \leq 2\pi$ results in an afterglow peak flux with a scatter of $\Delta \lesssim 0.5$ dex. The structure through the polar-angle, $0 \leq \iota \leq \theta_\gamma$, results in a larger scatter for the peak afterglow flux of $\lesssim 1.3$ dex. For the scatter in flux density due to the rotational orientation, the deviation from the mean gradually reduces with time and follows the expected change in beaming angle; the flux changes by a factor $\lesssim 1 + (\Delta/2 - 1) \times \min[1, (t_d/t)]^{3/8}$, where t_d is the deceleration time, and t is the observer time since burst.

The jet's kinetic energy, as inferred via afterglow modelling, will be broader than that assumed from a simple uniform jet model. For our two fiducial models, we find the inferred kinetic energy distribution covers $\gtrsim 1$ dex in energy for a fixed γ -ray efficiency, η . More realistically, η would vary as a function of both the energy and Lorentz factor with θ and ϕ , where at lower Lorentz factors some fraction of the prompt photons dissipated within the jet will be reabsorbed (Kobayashi & Sari 2001; Kobayashi et al. 2002) and the effective η would be smaller. Higher energy regions may result in more efficient shocks (e.g. Kobayashi & Sari 2001; Gottlieb et al. 2019) and the η could be larger. Such properties would further broaden the inferred kinetic energy distribution from a jet with a fixed energy.

The core angle, θ_c , from the fits to the mean energy and Lorentz factor profiles for equations 1–3, see Table 1, returns a remarkably similar value to that inferred via modelling the afterglow jet-break time in Nativi et al. (2022) using the same simulation data but a rotationally averaged jet profile. For jet simulations such as these, the core or jet opening angle is often presented as the average angle within which material has $h\Gamma > 10$ (e.g. Nagakura et al. 2014). Using this method with our 3D simulations, we find a $\theta_{\text{average}} = 0.1058$ and 0.1278 rad for the th50 and gs50 models respectively. These are both larger than the values found via profile fitting or the jet-break time by a factor ~ 2.5 – 3 . This suggests that the apparently narrower jets from our simulations are merely a result of the way θ_c is estimated. Such narrow jets are well within the observed range for opening angles⁴ inferred from the short GRB population (e.g., Jin et al. 2018; Lamb et al. 2019).

The degree of the jet collimation for a GRB producing jet, and the resultant jet opening angle is a complicated function of the jet's power, the density of the medium through which the jet is propagating, and the jet's initial opening angle (Bromberg et al. 2011). The details of how to estimate the final jet opening angle from a set of initial conditions and for an expanding medium are described by Hamidani & Ioka (2021), (see also Murguia-Berthier et al. 2017; Salafia et al. 2020, etc.). The degree of collimation is shown to be dominantly proportional to the ratio of jet power and ambient medium mass, $\theta/\theta_0 \propto (L_j/M_a)^{1/4}$, where θ is the resultant opening angle, θ_0 is the injected jet's opening angle, L_j is the jet power,

⁴ The opening angle inferred via the jet-break time of a GRB afterglow typically assumes that the observer is on the jet central axis. More detailed studies of the GRB population indicate that the typical inclination for an observed GRB is 0.57 of the jet's effective opening angle, θ_c in our notation, (Ryan et al. 2015). This suggests that the jet opening angle for GRBs are typically smaller by a factor ~ 0.64 than the simple estimates (Lamb et al. 2021).

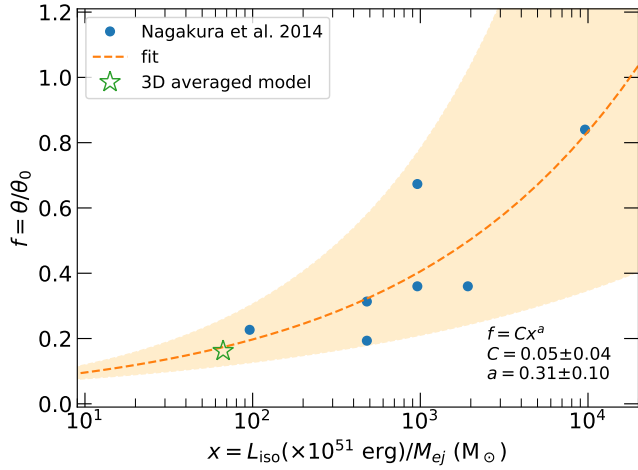


Figure 7. A fit to the ratio of jet power with ejecta mass and the degree of collimation for GRB jets from neutron star mergers. We use the results from 2D simulations in Nagakura et al. (2014) (blue circles) for our fit (orange dashed line), and show where our averaged fiducial jet profile fits on this plot (green star). The shaded region shows the $a = 0.31 \pm 0.10$ range. Note – our fiducial jet was not used in the fitting process.

and $M_a \equiv M_{ej}$ is the mass of the ambient medium/winds through which the jet is propagating and equivalent to the ejecta mass for a neutron star merger. The exact relation depends on how the medium is expanding, the ratio of the energy density for the jet to ejecta, and weakly on the timescale. Additionally, particle effects such as neutron conversion-diffusion may contribute to the resultant jet structure (Preau et al. 2021).

The afterglows to short GRBs indicate that they are accompanied by a broad diversity of kilonovae (e.g. Gompertz et al. 2018; Rossi et al. 2020). Model fits to GRB afterglows with kilonova candidates suggest that the population ejecta mass distribution has a scatter of $\Delta \log M_{ej} \lesssim 1$, a broad uncertainty on the ejecta velocity, $v_{ej} \leq 0.3c$, and a several orders of magnitude range for the Lanthanide fraction (Ascenzi et al. 2019). Theoretical studies of kilonova models show an equally diverse range of possible parameters (e.g. Kawaguchi et al. 2020). The mass and velocity of the ejecta, and the power and initial opening angle of the jet have an influence on the resulting jet opening angle – to approximate these factors, we take the results of 2D hydrodynamic simulations for a variety of initial jet and ejecta compositions from Nagakura et al. (2014) and fit a power-law function, $\theta/\theta_0 \propto (L_j/M_{ej})^a$, to determine the index a for the scaling. The results are shown in Figure 7, where we have used the isotropic equivalent luminosity for the initial jet. The opening angle, as inferred from jet profile fitting, for our averaged jet structure model is shown as a star. The fit index $a = 0.31 \pm 0.10$ is within error of the theoretically expected, $a = 0.25$, where we ignore the timescale and ejecta expansion dependence (Hamidani et al. 2020).

Using the fit shown in Figure 7, the core angle for a structured jet with our ‘Averaged’ jet profile, as a function of the core energy and the ejecta mass, is

$$\theta_c = 0.0424 \left[\frac{E_{c,iso}/1.9 \times 10^{52} \text{ erg}}{M_{ej}/0.072 M_\odot} \right]^{0.31} \text{ rad}, \quad (6)$$

where $E_{c,iso}$ is the isotropic equivalent total energy for the jet on the jet central axis i.e., $\theta = 0$, and M_{ej} is the mass of the ejecta/wind.

4.1 Comparison to sources with kilonova candidates

Figure 6 shows our sample of 30 composite short GRB afterglows normalised to $z = 1$ (Kann et al. 2011; Agüí Fernández et al. 2021). The GRBs with kilonova candidates within this sample have coloured lines, points marking the data, and a corresponding legend identifier. These kilonova candidate GRBs are additionally listed in Table 2, with the literature values for merger ejecta masses inferred from model fits/estimates to observations by the listed reference.

Figure 8 shows the 9 kilonova candidate GRB afterglows in our sample. Each panel includes an afterglow generated using our ‘Averaged’ jet structure profile with the core size, θ_c , reevaluated using equation 6 with the first ejecta mass estimate listed in Table 2 for the relevant GRB. Model lightcurves shown as red lines have fixed microphysical parameters, $\sqrt{\epsilon_B} = \epsilon_e = 0.1$, an index p value from literature for each GRB as listed in Table 2, and where the model lightcurve is shown with a green line, we change to $\epsilon_B = 0.1$ to give better agreement with the data. For each lightcurve we vary the value of the ambient density to find an approximate alignment between our fiducial model and the afterglow data⁵. For GRBs 050724, 080905A, and 160821B, we could not find a satisfactory alignment using our total jet energy and varying only the ambient density. However, as described in Lamb et al. (2019), GRB 160821B requires an initially low-power jet that is refreshed at later times⁶. The equivalent energy of the initial jet in GRB 160821B is ~ 0.1 that of our fiducial jet, however, the energy injection at $\gtrsim 1$ days for GRB 160821B results in a total energy that is consistent with the energy of our single episode jet model (see Lamb et al. 2019, for details). We apply this same reduction in initial jet energy to GRBs 050724 and 080905A to achieve a better alignment with the observed flux density. Our model lightcurves do not include the refreshed shock contribution, however, for GRB 160821B this is equivalent to the late time ‘excess’ seen in the data. No data, other than the non-constraining upper-limits, at $\gtrsim 10$ days is available for GRBs 050724 or 080905A to test the refreshed shock scenario.

The model afterglows in Figure 8 also show the maximum variability due to the rotational orientation of the jet with respect to the observer, as shown in Figure 3 – note that this uncertainty in peak flux does not affect the on-axis case. The angle θ_γ provides an indication of the highest angle from which an observable GRB is likely to be emitted, however, this is not a hard limit and where beaming effects, the distance to the source, and secondary γ -ray emitting components are considered e.g. shock breakout of the cocoon, then the inclination at which an observer could detect the GRB is higher for nearby sources.

The lightcurves for GRBs 050724, 060614 and 150424A stand out in our sample as having a late break to the steep decline phase when compared with our fiducial models, and the green lightcurves shown in Figure 8 have used $\epsilon_B = 0.1$ to give better agreement with the data – additionally noting that the choice of initial jet energy

⁵ A sophisticated fit to these data sets would require the inclusion of reverse shock emission, refreshed shock or energy injection, plus a kilonova contribution. This is beyond the scope of this work, however, using the literature values of the index p , should ensure that our approximate lightcurve models are consistent with any X-ray afterglow flux for individual bursts. Other works have focused on fitting afterglow and kilonova models to data e.g. Ascenzi et al. (2019).

⁶ The data presented here for GRBs 130603B and 160821B has the kilonova dominated data removed (see Tanvir et al. 2013; Lamb et al. 2019), however, all other GRBs in our sample may include multiple emission components and, potentially, a significant contribution from a kilonova.

Table 2. Short GRBs with kilonova candidates. Estimated ejecta masses are from the respective reference column – where more than one mass is listed, the values are in the reference order; the bold value is that used to determine the jet collimation for the models shown in Figure 8. GRBs 150101B and 200522A, below the line, are not included in our optical lightcurve sample. The 4th and 5th columns show the value of index p used for the model afterglow lightcurves, and the relevant reference. The last three columns show the opening angle, the isotropic equivalent kinetic energy, inferred from the jet structure in each case, and the ambient particle density used for the lightcurves in Figure 8.

GRB	M_{ej} (M_{\odot})	Ref.	p	Ref.	θ_c	$E_k \times 10^{52}$ erg	$\log n \text{ cm}^{-3}$
050709	0.05	[1] [2]	2.31	[10]	0.047	1.81	-3.00
050724*	0.001	[3]	2.29	[10]	0.078	0.07	-1.00
060614	0.077 , 0.1	[2] [1]	2.40	[11]	0.042	2.28	-3.30
061006	0.01	[3]	2.39	[10]	0.078	0.66	-2.92
070714B	0.01	[3]	2.30	[10]	0.078	0.66	-1.00
080905A*	0.007	[2]	2.06	[10]	0.087	0.05	-2.15
130603B	0.03 , 0.01–0.1, 0.075	[1] [4] [2]	2.70	[10]	0.056	1.28	-1.00
150424A	0.1	[2]	2.30	[2]	0.040	2.50	-1.40
160821B*	0.01 , 0.17, <0.006	[7], [2], [8]	2.30	[7]	0.078	0.66	-2.00
150101B	>0.02, >0.1, 0.037	[5] [6] [2]	–	–	–	–	–
200522A	0.1	[9]	–	–	–	–	–

[1] Jin et al. (2016), [2] Ascenzi et al. (2019), [3] Gao et al. (2017), [4] Tanvir et al. (2013), [5] Troja et al. (2018), [6] Fong et al. (2016), [7] Lamb et al. (2019), [8] Troja et al. (2019) [9] Fong et al. (2021) [10] Fong et al. (2015) [11] Jin et al. (2015)

* indicates a GRB where we reduced our jet model energy by a factor 10

in our simulation was arbitrary⁷. The opening angle for these jet models relies on the ejecta mass estimates, and for GRB 050724, the value of $0.001 M_{\odot}$ is the smallest in our sample and may well be underestimated. GRB 060614 is technically a long-duration GRB, with a prompt burst episode lasting ~ 100 s, however, the absence of an accompanying bright supernova combined with it exhibiting an initial spike of gamma-rays with a duration of only a few seconds has led to speculation that it could have been produced by a compact binary merger (Gal-Yam et al. 2006; Gehrels et al. 2006; Perley et al. 2009; Kann et al. 2011). The differences in these GRBs (noting that GRB 150424A which has a large uncertainty on the source redshift e.g. Knust et al. 2017) may indicate that these bursts have a different progenitor to typical short GRBs i.e. they may be the result of a neutron star-black hole merger as opposed to a binary neutron star merger (e.g. Gompertz et al. 2020), where the potential energy budget for the jet is marginally higher (e.g. Shapiro 2017).

The compact stellar merger origin for short GRBs has a limited energy budget for the jets, typically of the order $\sim 10^{51}$ erg for neutron star mergers (Fryer et al. 2019). Yet the observed distribution for the energy in the short GRB population spans ~ 4 orders of magnitude, see Figure 4 and Fong et al. (2015). Here we have shown that inhomogeneity in the energy and velocity distribution across an emergent jet’s surface due to turbulent processes via jet-ejecta mixing can account for a significant fraction of the observed spread in inferred kinetic energies. By taking into account the range of ejecta masses from the candidate kilonova population, the effective opening angle (the jet core angle in our notation) for a GRB jet with a fixed, or limited, energy budget can be determined. When combined with the expected variation in the ambient density between sources we can explain much of the variety in afterglow flux and timescales for the small sample of GRBs with kilonova candidates. The isotropic equivalent kinetic energy for each afterglow structure, given the fixed initial jet energy and the model core angle is shown in Table 2 – the range of energy values here are ~ 3 orders of magnitude and when combined with the additional order of magnitude spread due to inclination reflects the full range seen in the short GRB population.

Figure 2, where $\iota \sim 4 - 5\theta_c$, and fits for the rotationally averaged simulation jet structure profiles in Nativi et al. (2022) show that such a functional jet structure is additionally consistent with the afterglow of GW170817/GRB 170817A – we do not repeat that analysis here. For the afterglow to GRB 170817A, multiple jet structure profiles have shown viable fits to the data, including more exotic structures than the core-dominated profiles presented here (e.g., Takahashi & Ioka 2021), as well as the refreshed shock/energy injection scenario (Lamb et al. 2020).

5 CONCLUSIONS

We have demonstrated that the inhomogeneity in energy and velocity across the jet surface of a 3D hydrodynamic jet-neutron star merger wind simulation results in a peak afterglow flux density that depends on the observer-system orientation relative to the jet central axis in terms of both polar and rotation angles. The potential change in peak flux with orientation within a γ -ray emitting region of a jet with a fixed total energy results in:

- Variation in peak afterglow flux density due to rotation, < 0.5 dex.
- Variation in peak afterglow flux density due to inclination (polar orientation), < 1.3 dex.
- An order of magnitude spread in jet kinetic energy distribution when inferred from the peak afterglow, where the γ -ray efficiency of the GRB emission is fixed.

We define a physically motivated analytic function for a typical neutron star merger jet, and demonstrate how, for a given jet energy and merger ejecta mass, the effective opening angle of the jet can change. Using the literature reported ejecta masses for six candidate kilonovae, we show that a fixed injected jet energy ($E_{\text{iso}} \sim 6 \times 10^{50}$ erg) with our analytic structure function can account for the diversity of observed afterglow lightcurves by changing only the ambient medium density. For a further three GRB-kilonova candidates in our sample; GRBs 050724, 080905A, and 160821B, we find that the jet energy of our fiducial model must be reduced by an order of magnitude. This reduction is consistent with the refreshed shock scenario used to describe the afterglow of GRB 160821B in Lamb et al. (2019), where the total, post-injection energy of the afterglow is

⁷ The isotropic equivalent energy of the injected jets are $\sim 6 \times 10^{50}$ erg, and slightly lower than the $\sim 10^{51}$ erg expected for mergers (Shapiro 2017; Fryer et al. 2019)

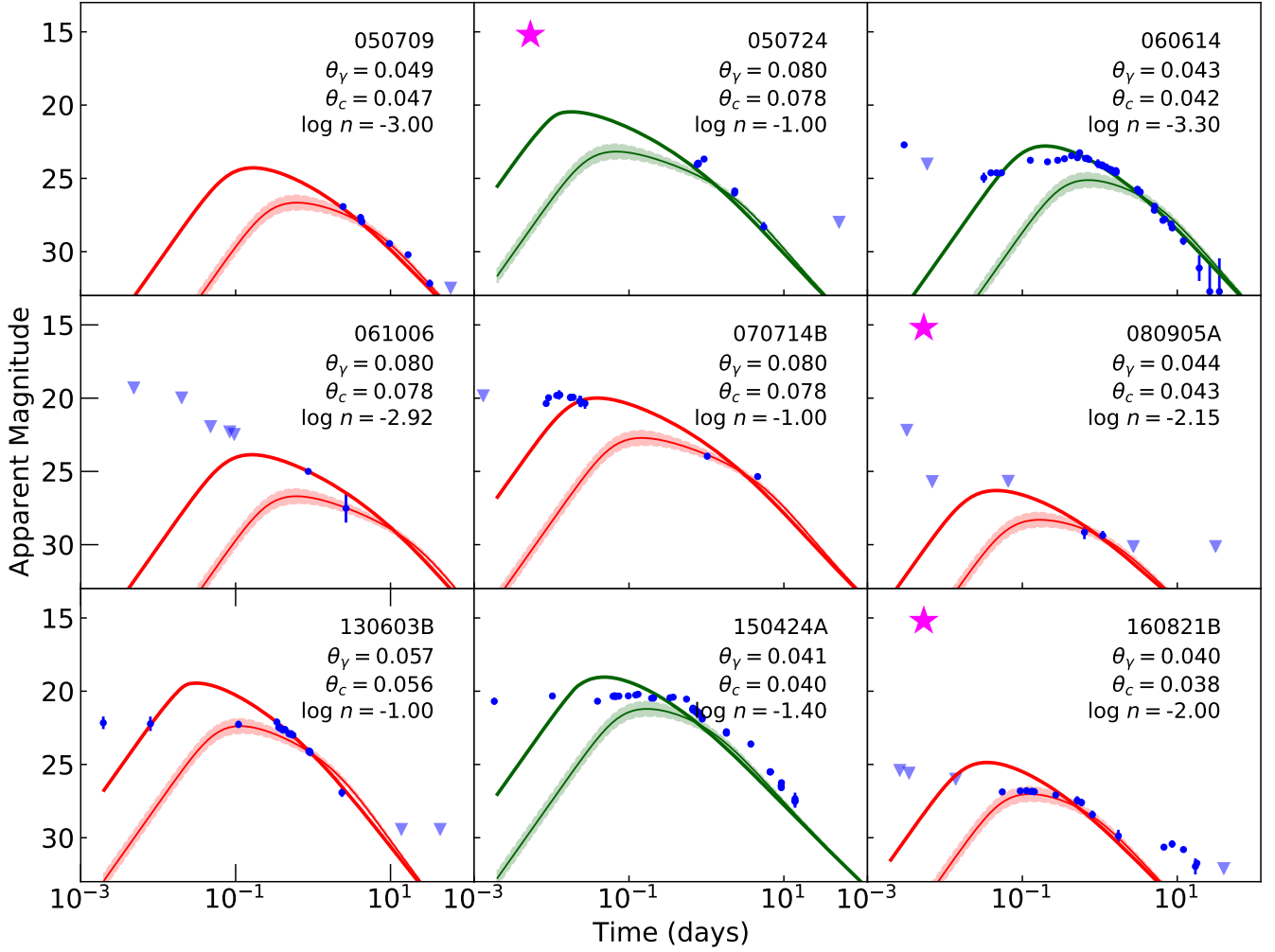


Figure 8. GRBs in our sample with candidate kilonova claims in the literature. Our afterglow model with a fixed energy is shown to be consistent with the observed lightcurves. In each case we modify the jet structure profile with the candidate kilonova’s reported eject mass, and vary the ambient medium to give a satisfactory alignment between the $0 \leq \iota \leq \theta_\gamma$ for the lightcurves, thick and thin red/green lines respectively. Lightcurves in green have $\epsilon_B = 0.1$ instead of the fiducial, $\epsilon_B = 0.01$. Each panel shows θ_γ , θ_c , and the $\log n$, where n is given in cm^{-3} . Panels marked with a pink star (GRBs 050724, 080905A, and 160821B) have a reduced energy (by a factor 0.1) to better describe the observed afterglows. Note – afterglow parameters are not fits to the data, and the afterglow models do not include the kilonova, reverse shock, or energy injection contribution.

equivalent to that of our fiducial model. This indicates that the intrinsic energy range for the short GRB population is likely very narrow, and consistent with the theoretical prediction for neutron star merger central engines.

ACKNOWLEDGEMENTS

GPL thanks Fergus Hayes, En-Tzu Lin, Laurence Datrier, Surojit Saha, Michael Williams, Siong Heng, Martin Hendry, Albert Kong, and John Veitch for useful discussions via online meetings throughout 2020–2021. GPL is supported by STFC grant ST/S000453/1. DAK acknowledges support from Spanish National Research Project RTI2018-098104-J-I00 (GRBPhot). SR and LN were supported by the Swedish Research Council (VR) under grant number 2016_03657, by the Swedish National Space Board under grant number Dnr. 107/16, by the research environment grant “Gravitational Radiation and Electromagnetic Astrophysical Transients

(GREAT)” funded by the Swedish Research council (VR) under Dnr 2016_06012 and by the Knut and Alice Wallenberg Foundation under grant Dnr. KAW 2019.0112. The hydrodynamic simulations were performed on resources provided by the Swedish National Infrastructure for Computing (SNIC) at Beskow.

DATA AVAILABILITY

Data available on reasonable request.

REFERENCES

- Agüí Fernández J. F., et al., 2021, arXiv e-prints, [p. arXiv:2109.13838](https://arxiv.org/abs/2109.13838)
- Aksulu M. D., Wijers R. A. M. J., van Eerten H. J., van der Horst A. J., 2021, arXiv e-prints, [p. arXiv:2106.14921](https://arxiv.org/abs/2106.14921)
- Aloy M. A., Janka H. T., Müller E., 2005, *A&A*, **436**, 273
- Ascenzi S., et al., 2019, *MNRAS*, **486**, 672

- Beniamini P., Nakar E., 2019, *MNRAS*, **482**, 5430
- Beniamini P., Granot J., Gill R., 2020, *MNRAS*, **493**, 3521
- Berger E., 2014, *ARA&A*, **52**, 43
- Bromberg O., Nakar E., Piran T., Sari R., 2011, *ApJ*, **740**, 100
- D'Avanzo P., 2015, *Journal of High Energy Astrophysics*, **7**, 73
- Duffell P. C., Quataert E., MacFadyen A. I., 2015, *ApJ*, **813**, 64
- Fong W., Berger E., Margutti R., Zauderer B. A., 2015, *ApJ*, **815**, 102
- Fong W., et al., 2016, *ApJ*, **833**, 151
- Fong W., et al., 2021, *ApJ*, **906**, 127
- Fryer C. L., Lloyd-Ronning N., Wollaeger R., Wiggins B., Miller J., Dolence J., Ryan B., Fields C. E., 2019, *European Physical Journal A*, **55**, 132
- Gal-Yam A., et al., 2006, *Nature*, **444**, 1053
- Gao H., Zhang B., Lü H.-J., Li Y., 2017, *ApJ*, **837**, 50
- Gehrels N., et al., 2006, *Nature*, **444**, 1044
- Geng J.-J., Zhang B., Kölligan A., Kuiper R., Huang Y.-F., 2019, *ApJ*, **877**, L40
- Gompertz B. P., et al., 2018, *ApJ*, **860**, 62
- Gompertz B. P., Levan A. J., Tanvir N. R., 2020, *ApJ*, **895**, 58
- Gottlieb O., Levinson A., Nakar E., 2019, *MNRAS*, **488**, 1416
- Hamidani H., Ioka K., 2021, *MNRAS*, **500**, 627
- Hamidani H., Kiuchi K., Ioka K., 2020, *MNRAS*, **491**, 3192
- Hotokezaka K., Kiuchi K., Kyutoku K., Okawa H., Sekiguchi Y.-i., Shibata M., Taniguchi K., 2013, *Phys. Rev. D*, **87**, 024001
- Jin Z.-P., Li X., Cano Z., Covino S., Fan Y.-Z., Wei D.-M., 2015, *ApJ*, **811**, L22
- Jin Z.-P., et al., 2016, *Nature Communications*, **7**, 12898
- Jin Z.-P., et al., 2018, *ApJ*, **857**, 128
- Kann D. A., et al., 2011, *ApJ*, **734**, 96
- Kawaguchi K., Shibata M., Tanaka M., 2020, *ApJ*, **889**, 171
- Knust F., et al., 2017, *A&A*, **607**, A84
- Kobayashi S., Sari R., 2001, *ApJ*, **551**, 934
- Kobayashi S., Ryde F., MacFadyen A., 2002, *ApJ*, **577**, 302
- Lamb G. P., Kobayashi S., 2016, *ApJ*, **829**, 112
- Lamb G. P., Kobayashi S., 2017, *MNRAS*, **472**, 4953
- Lamb G. P., Mandel I., Resmi L., 2018, *MNRAS*, **481**, 2581
- Lamb G. P., et al., 2019, *ApJ*, **883**, 48
- Lamb G. P., Levan A. J., Tanvir N. R., 2020, *ApJ*, **899**, 105
- Lamb G. P., Kann D. A., Fernández J. J., Mandel I., Levan A. J., Tanvir N. R., 2021, *MNRAS*, **506**, 4163
- Lithwick Y., Sari R., 2001, *ApJ*, **555**, 540
- Matsumoto T., Nakar E., Piran T., 2019, *MNRAS*, **486**, 1563
- Murguia-Berthier A., et al., 2017, *ApJ*, **835**, L34
- Nagakura H., Hotokezaka K., Sekiguchi Y., Shibata M., Ioka K., 2014, *ApJ*, **784**, L28
- Nakar E., 2007, *Phys. Rep.*, **442**, 166
- Nathanail A., Gill R., Porth O., Fromm C. M., Rezzolla L., 2021, *MNRAS*, **502**, 1843
- Nativi L., Bulla M., Rosswog S., Lundman C., Kowal G., Gizzi D., Lamb G. P., Perego A., 2021, *MNRAS*, **500**, 1772
- Nativi L., Lamb G. P., Rosswog S., Lundman C., Kowal G., 2022, *MNRAS*, **509**, 903
- O'Connor B., Beniamini P., Kouveliotou C., 2020, *MNRAS*, **495**, 4782
- Pavan A., Ciolfi R., Kalinani J. V., Mignone A., 2021, *MNRAS*, **506**, 3483
- Perego A., Rosswog S., Cabezón R. M., Korobkin O., Käppeli R., Arcones A., Liebendörfer M., 2014, *MNRAS*, **443**, 3134
- Perley D. A., et al., 2009, *ApJ*, **696**, 1871
- Preau E., Ioka K., Mészáros P., 2021, *MNRAS*, **503**, 2499
- Rossi A., et al., 2020, *MNRAS*, **493**, 3379
- Rosswog S., Liebendörfer M., Thielemann F. K., Davies M. B., Benz W., Piran T., 1999, *A&A*, **341**, 499
- Ryan G., van Eerten H., MacFadyen A., Zhang B.-B., 2015, *ApJ*, **799**, 3
- Salafia O. S., Barbieri C., Ascenzi S., Toffano M., 2020, *A&A*, **636**, A105
- Sari R., Piran T., Narayan R., 1998, *ApJ*, **497**, L17
- Shapiro S. L., 2017, *Phys. Rev. D*, **95**, 101303
- Takahashi K., Ioka K., 2021, *MNRAS*, **501**, 5746
- Tanvir N. R., Levan A. J., Fruchter A. S., Hjorth J., Hounsell R. A., Wiersema K., Tunnicliffe R. L., 2013, *Nature*, **500**, 547
- Troja E., et al., 2018, *Nature Communications*, **9**, 4089
- Troja E., et al., 2019, *MNRAS*, **489**, 2104
- Urrutia G., De Colle F., Murguia-Berthier A., Ramirez-Ruiz E., 2021, *MNRAS*, **503**, 4363

This paper has been typeset from a \LaTeX file prepared by the author.